



Low-consumption water purification: Trace H_2O_2 triggering H_2O_2 generation through pollutant utilization on non-equilibrium ZnS surface

Chao Lu^a, Chun Hu^a, Hongwei Rong^b, Lai Lyu^{a,c,*}

^a Institute of Environmental Research at Greater Bay, Key Laboratory for Water Quality and Conservation of the Pearl River Delta, Ministry of Education, Guangzhou University, Guangzhou 510006, China

^b School of Civil Engineering, Guangzhou University, Guangzhou 510006, China

^c Institute of Rural Revitalization, Guangzhou University, Guangzhou 510006, China

ARTICLE INFO

Keywords:

Water purification
Oxygen reduction
 H_2O_2 generation
Heterogeneous catalysis
Waste valorization

ABSTRACT

A low-consumption water purification system is firstly constructed based on a new dual-reaction-center (DRC) catalyst molybdenum-doped zinc sulfide (Mo-ZnS, MZS) with a confined nonequilibrium surface. The extremely strong electron trapping ability of the Mo site is realized by the substitution of Mo for ZnS lattice. In this way, the electrons of emerging contaminants (ECs) are efficiently transferred to the nonequilibrium surface through the oriented interface process (Mo-S-Zn bond bridge), and obtained by the natural dissolved oxygen (DO) to generate hydrogen peroxide (H_2O_2) under trace H_2O_2 trigger without light and electricity assistant. The highest yield of H_2O_2 is even up to ~230 % of the initial value, and the ECs removal can reach 100 % within 60 min, which is far superior to conventional Fenton catalysts. This work realized the efficient utilization of the contaminant electrons through the construction of Mo-S-Zn bond bridge, which greatly reduced the energy consumption of water purification and improved the resourcefulness of ECs.

1. Introduction

Water purification currently suffers from overloaded treatment capacity and complicated composition of ECs, including endocrine disrupting chemicals (EDCs), persistent organic pollutants (POPs), antibiotics, microplastics, synthetic dyestuff, and others [1–4]. In China alone, the total amount of urban and rural wastewater emissions in 2020 exceeded 67.5 billion tons, with an annual growth of nearly 2 billion tons. Traditional municipal wastewater treatment technology has difficulty for removing ECs, even with excessive resources and energy consumption [5,6]. Previous studies have shown that advanced oxidation processes (AOPs) possess viable capability for the removal of refractory organic compounds [7–11]. The Fenton reaction, one of the most widely used AOPs (~70 %), generates reactive oxygen species (ROS, including $\text{O}_2^{\cdot-}$, $\cdot\text{OH}$ and $^1\text{O}_2$) through the oxidation and reduction of H_2O_2 that can rapidly attack pollutant structures, has become a promising technology for pollutant removal. However, the large amount of H_2O_2 consumed by the reaction cycle has become the biggest bottleneck for the application of this technology [12].

H_2O_2 is a versatile chemical widely used in synthesis, medical

disinfection, and wastewater treatment [13–16]. Large-scale industrial synthesis of H_2O_2 is performed via the ethyl anthraquinone method, a multistep reaction process that requires the participation of precious metal catalysts, consumes large amounts of energy and resources, and is accompanied by the generation of organic wastewater [17]. Direct synthesis of H_2O_2 using hydrogen (H_2) and oxygen (O_2) has emerged as an environmentally friendly alternative [18–21]. However, this process carries a high risk of explosion, and the yield remains low, leading to significant challenges for practical applications. The two-electron oxygen reduction reaction (2e^- ORR) has received widespread attention due to the simplicity of the reaction process and mild reaction characteristics [22,23]. To deliver the electrons of sacrificial agents to inert ground state O_2 and break the energy barrier from O_2 to H_2O_2 , this process always requires the assistance of external energy, such as electricity or light [24–27]. Generally, this process is high in consumption and low in efficiency, resulting in a significant waste of resources and energy. Thus, considerable work has been conducted to overcome these drawbacks [28–33]. However, the reliance of traditional mechanisms on external energy and sacrificial agents is the largest bottleneck in energy savings and consumption reduction. New ways of supplying electrons or energy

* Corresponding author at: Institute of Environmental Research at Greater Bay, Key Laboratory for Water Quality and Conservation of the Pearl River Delta, Ministry of Education, Guangzhou University, Guangzhou 510006, China.

E-mail address: lyulai@gzhu.edu.cn (L. Lyu).

<https://doi.org/10.1016/j.apcatb.2023.123051>

Received 21 February 2023; Received in revised form 9 June 2023; Accepted 26 June 2023

Available online 28 June 2023

0926-3373/© 2023 Elsevier B.V. All rights reserved.

may be able to solve this problem.

In our previous work, electron-rich organic pollutants, typically regarded as unusable and harmful materials, were found to be the dominant electron donors in Fenton-like reaction systems [34–37]. By regulating the distribution of electrons and constructing electron-poor/electron-rich microregions like primary cells on the catalyst surface, the application of pollutant electrons instead of sacrificial agents in $2e^-$ ORR may be achieved. In this process, pollutants are usually specifically adsorbed into the electron-poor region for directional and continuous electron donation to the system via cation- π and π - π interactions [38–41]. Subsequently, the electrons are transferred to the electron-rich region to equilibrate the consumption in activating peroxides [42]. In some systems, electrons donated by electron-rich regions can be even used for oxygen reduction [43]. In addition, the

construction of suitable DRCs by exploiting the driving force, can further reduce or even eliminate the dependence on external energy. This provides a new method to solve the high energy consumption challenge created by the ORR reaction. Although the surface structure of catalysts that can utilize pollutant electrons for the ORR still remains unclear, the construction of suitable DRCs to match the energy barriers of $2e^-$ ORR offers hope and possibility, which is often associated with d -block metals [44].

Herein, based on this hypothesis, we present a novel type of DRCs catalyst (Mo-ZnS) characterized by a confined nonequilibrium surface for rapidly removing ECs from water and simultaneously generating H_2O_2 without light and electricity, relying only on trace H_2O_2 triggering. The structural features and electron distribution of MZS were investigated using a series of characterization and density functional theory

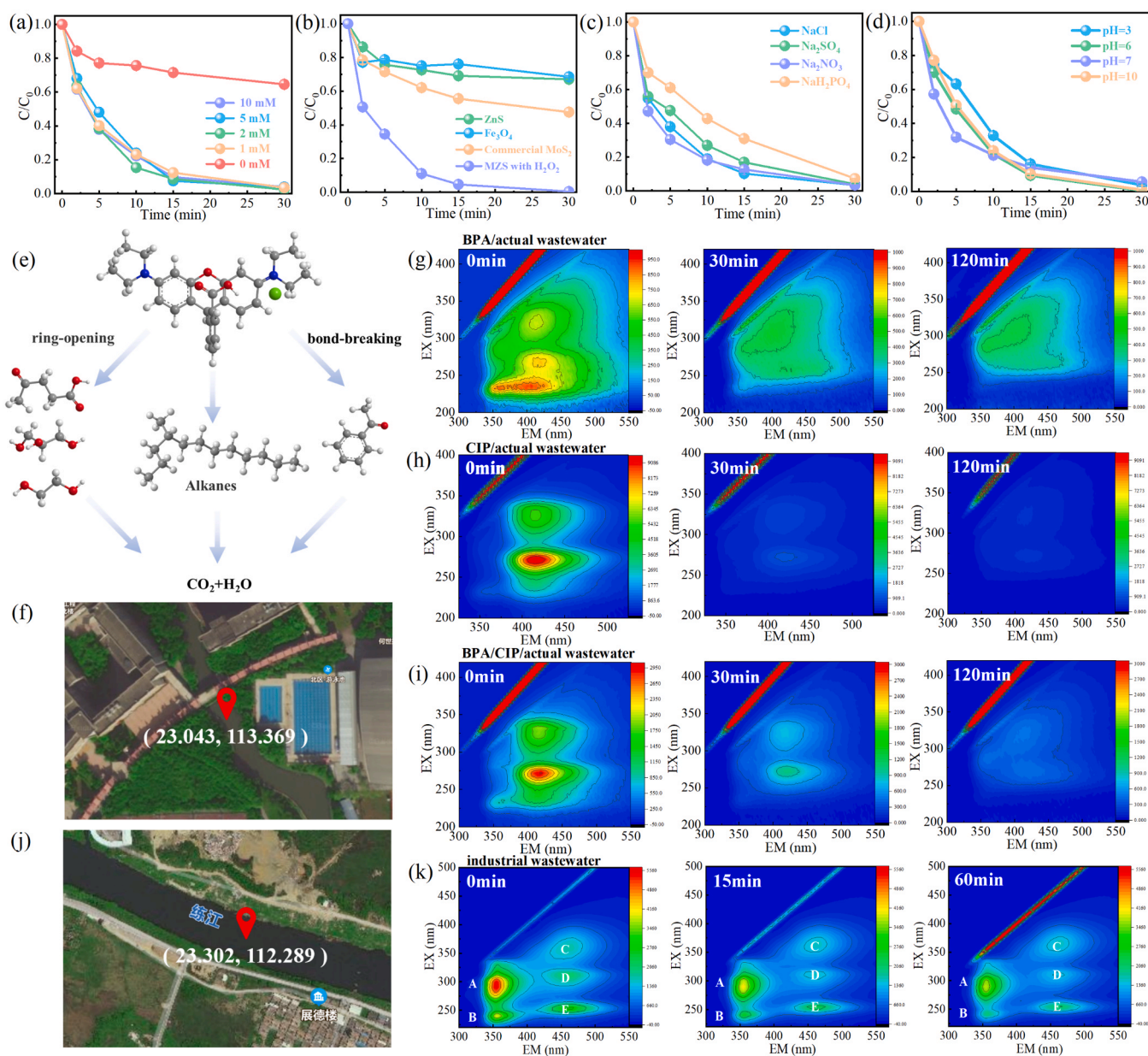


Fig. 1. Pollutant degradation curves in (a) various H_2O_2 concentration suspensions and (b) various catalyst suspensions. Effect of (c) salts and (d) initial pH values for pollutant degradation in the MZS/ H_2O_2 system. (e) Analysis of RhB degradation pathways. (f) Actual wastewater intake point. 3D-EEM fluorescence spectroscopy of (g) BPA/actual wastewater, (h) CIP/actual wastewater, and (i) BPA/CIP/actual wastewater samples after reaction with MZS/ H_2O_2 over different time periods. (j) Industrial wastewater intake point and (k) 3D-EEM fluorescence spectroscopy of corresponding water samples. Reaction conditions: [catalyst] = 0.2 g/L (Mo and Zn with the same metal content in b), [pollutant] = 10 mg/L 50 mL (1 mg/L 50 mL for g, h and i), [H_2O_2] = 10 mM (except a, and 1 M H_2O_2 for g, h and i), initial pH \approx 6.2 (except c), [concentration of salts] = 0.1 mol/L. Error bars = standard deviation ($n = 3$).

(DFT) calculations. During the Fenton-like reaction of MZS, the reinforced DRCs driven by trace H_2O_2 are able to utilize pollutant electrons and DO for efficient pollutant removal and simultaneous H_2O_2 generation. In addition, this system is nearly unaffected by variations in pH and salinity, showing good adaptability to complex environments. A novel heterogeneous interface reaction mechanism involving catalyst/ECs/ $\text{DO}/\text{H}_2\text{O}_2$ is proposed in this work, providing a new perspective to solving the high energy consumption problem of water purification and ORR.

2. Experimental section

MZS was prepared through an enhanced hydrothermal one-pot synthesis method. Typically, $(\text{CH}_3\text{COO})_2\text{Zn}$, $(\text{NH}_4)_6\text{Mo}_7\text{O}_{24} \cdot 4 \text{H}_2\text{O}$ and $\text{CH}_4\text{N}_2\text{S}$ were mixed at a fixed temperature in deionized water, followed by alternately stirring and sonication to form the MZS-precursor. Then the enhanced hydrothermal reaction was conducted in a reaction autoclave to promote the growth of nucleus and the formation of chemical structure to obtain semi-manufactured MZS. Several washes with ethanol and water were required to remove possible by-products. The obtained solid was the target material MZS. The details of chemicals, synthesis procedure and characterizations are shown in [Supporting Information \(SI\)](#).

3. Results and discussion

3.1. Performance of MZS/ H_2O_2 system for ECs degradation

The as-prepared catalysts were coupled with H_2O_2 to construct a Fenton-like system (MZS/ H_2O_2) to degrade typical refractory pollutants, such as pesticides, pharmaceuticals, and dyes, under natural conditions. The structure and degradation results are shown in [Fig. S1](#) and [Fig. S2](#), respectively. Optimal degradation experimental conditions were explored ([Fig. S3](#)). MZS/ H_2O_2 could rapidly remove pollutants under the trigger of various H_2O_2 concentrations, even at the extremely low concentration of 1 mM ([Fig. 1a](#)). When there was no H_2O_2 present in the system, MZS alone was also able to remove 35.4 % of rhodamine b (RhB) within 30 min, which could be attributed to the adsorption of pollutants on the MZS surface and the decolorization effect of ROS generated by DO activation due to the efficient piezoelectric properties of MZS. As shown in [Fig. 1b](#), only 31.5 % of RhB was decolorized at 30 min in the common metal oxide $\text{Fe}_3\text{O}_4/\text{H}_2\text{O}_2$ system. In contrast, pollutants were decolorized extremely quickly in the MZS/ H_2O_2 system. The degradation rate reached as high as 88.9 % within only 10 min and reached ~100 % at 30 min. Even within the initial two minutes, ~50 % of pollutants were degraded in this innovative system. In contrast, only 32.9 % and 52.4 % of pollutants were decolorized within 30 min in the $\text{ZnS}/\text{H}_2\text{O}_2$ and commercial $\text{MoS}_2/\text{H}_2\text{O}_2$ systems, respectively. These results proved that the construction of a confined nonequilibrium surface on MZS resulted in excellent Fenton-like activity for ECs removal. After six experimental cycles, the degradation rate of RhB remained above 97 %, demonstrating the excellent repeatability of the MZS/ H_2O_2 system ([Fig. S4](#)). Due to the high salinity and complex pH range of actual wastewater, the activity of MZS/ H_2O_2 under different salt conditions and pH values was investigated [45]. The effect of salinity on the degradation of pollutants showed that MZS/ H_2O_2 could maintain excellent activity in high concentrations (0.1 mol/L) of a variety of salts, including chlorates, sulfates and phosphates. The RhB was nearly completely degraded within 30 min, indicating that MZS/ H_2O_2 could adapt to various complex salt environments ([Fig. 1c](#)). Similarly, the degradation activity of MZS/ H_2O_2 for RhB was also tested in highly acidic, neutral, and alkaline conditions. The results demonstrated that the removal of pollutants by MZS/ H_2O_2 was nearly unaffected by pH over the wide range of pH 3–10 and achieved nearly complete degradation in 30 min. This effectively overcame the disadvantage of the narrow pH range required by heterogeneous Fenton-like catalysts ([Fig. 1d](#)). A large amount of ring-opening and

bond-breaking production proved that the pollutant was effectively removed under trace H_2O_2 triggering ([Fig. 1e](#)). To verify the removal effect of MZS/ H_2O_2 on actual wastewater, degradation experiments in actual water (obtained from Guangdong Province, [Fig. 1f](#)) were carried out. Functional group disruptions of bisphenol A (BPA) ([Fig. 1g](#)) and ciprofloxacin (CIP) ([Fig. 1h](#)) could be clearly observed with the help of three-dimensional excitation and emission matrix (3D-EEM) fluorescence spectroscopy, even with H_2O_2 triggering at low concentration of only 1 mM (2 mM is shown in [Fig. S5](#)). In particular, the CIP/actual wastewater was nearly fully removed within 30 min. Moreover, the synergy of CIP and BPA could also promote the degradation of BPA, indicating that MZS/ H_2O_2 could maintain excellent performance in actual water with a complex composition ([Fig. 1i](#)). Biologically treated industrial wastewater from a dyeing and printing industrial park in Guangdong Province, China ([Fig. 1j](#), the specific industrial park was not mentioned due to confidentiality requirements) was employed to further test the practicality of MZS/ H_2O_2 . Due to the difference in fluorescence sensitivity of pollutants in the wastewater, which were associated with dye-based substances of poor biodegradability ([Fig. 1k](#)), 3D-EEM fluorescence spectroscopy of the raw wastewater sample resulted in five main peaks located at 260–340/330–390 nm (peak A), 220–260/330–380 nm (peak B), 340–380/435–480 nm (peak C), 290–325/420–490 nm (peak D), and 240–265/410–505 nm (peak E) Ex/Em. All peaks were found to be significantly weakened after treatment with MZS/ H_2O_2 , proving the suitability of MZS/ H_2O_2 for treating actual wastewater with complex composition.

3.2. Key role of ECs in H_2O_2 generation

The shade treatment was performed to exclude the visible light response of MZS. As shown in the [Fig. S6](#), there was almost no effect on pollutant degradation rate and ORR performance with the presence or absence of visible light. No H_2O_2 generation was detected in the MZS/pollutant system through the DPD-PDO method, which was attributed to the extremely small amount of H_2O_2 generated by oxygen reduction and the preference of the generated H_2O_2 to be activated to ROS on MZS surface. Throughout the entire MZS/RhB/ H_2O_2 reaction, the H_2O_2 concentration was observed to fluctuate in a sawtooth pattern with small amplitude ([Fig. 2a](#)). By itself, MZS decomposed H_2O_2 extremely slowly ([Fig. 2b](#)), thereby showing that MZS maintains an extremely high H_2O_2 utilization. Combined with the degradation curve, the H_2O_2 concentration remained above 94 % of the initial level over 30 min, likely owing to pollutant occupying more active sites to donate electrons to the system to enable the 2e^- ORR process to generate H_2O_2 without using light or electricity. In contrast, the H_2O_2 concentration decreased slowly after the complete degradation of RhB, showing the relatively poor electron donation capacity of RhB intermediates, which results in less H_2O_2 generation. In particular, the H_2O_2 concentration detected was 112.3 % of the initial level at 2 min, demonstrating that there was indeed H_2O_2 generation in the MZS/ H_2O_2 system. Due to the poor Fenton-like activity of ZnS, the H_2O_2 consumption in the $\text{ZnS}/\text{H}_2\text{O}_2$ system was also extremely slow, with an overall decreasing trend and no sawtooth fluctuations. However, the decomposition of H_2O_2 in the commercial $\text{MoS}_2/\text{H}_2\text{O}_2$ system was remarkably rapid, indicating the extremely low utilization of H_2O_2 . Based on the analysis of pollutants and H_2O_2 concentrations during the reaction of the MZS/ H_2O_2 system, differences in the electron donation capacity of pollutants and intermediates were found. To verify this conjecture, 2-CP was selected as the new target ECs. As illustrated by the variation of the H_2O_2 concentration curve, the highest concentration of H_2O_2 (11.7 mM) was ~230 % of the initial concentration (5 mM), demonstrating the extremely strong electron donation effect of 2-CP for the 2e^- ORR process that generates H_2O_2 ([Fig. 2c](#)). It was worth noting that the 2-CP system presented larger sawtooth fluctuations throughout the entire process, proving that the structures of the ECs can directly affect the electron supply capacity. The C/C_0 of H_2O_2 in the 2-CP system was in large part lower than that in the

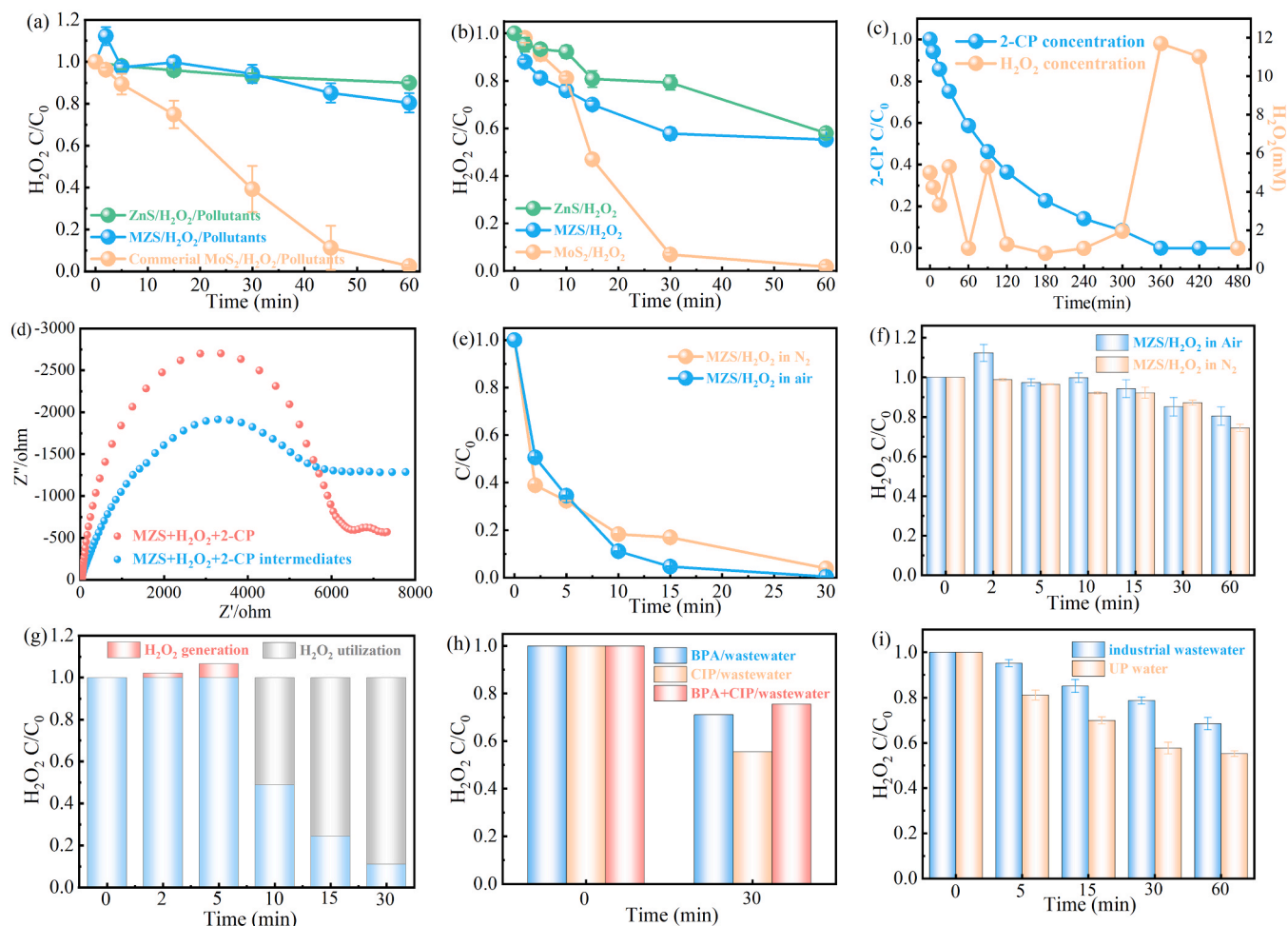


Fig. 2. Variation curves of H_2O_2 concentration in various (a) pollutant suspensions and (b) UP water suspensions. (c) 2-CP degradation curve and variation curves of H_2O_2 concentration. (d) Electrochemical impedance spectra (EIS) curves of the MZS/ H_2O_2 /2-CP and MZS/ H_2O_2 /2-CP intermediates. Effect of N_2 and air on the degradation of (e) RhB and (f) histogram of H_2O_2 concentration variation in the MZS/ H_2O_2 system. Histogram of H_2O_2 concentration variation in the MZS/ H_2O_2 system with (g) RhB, (h) various ECs/actual wastewater and (i) industrial wastewater and UP water. Reaction conditions: [catalyst] = 0.2 g/L, [pollutant] = 10 mg/L 50 mL (1 mg/L 50 mL for h), $[\text{H}_2\text{O}_2]$ = 10 mM (5 mM for c, 2 mM for g and h), initial $\text{pH} \approx 6.2$. Error bars = standard deviation ($n = 3$).

RhB system before 2-CP was completely degraded (within 300 min), indicating that the electron donation capacity of RhB was significantly stronger than that of 2-CP. With the nearly complete degradation of 2-CP to 2-CP intermediates (300 min), the H_2O_2 generated by the 2e^- ORR process reached its highest value due to the obviously stronger electron donation ability of 2-CP intermediates. Relevant electrochemical impedance spectroscopy (EIS) experiments were conducted to demonstrate the difference in electron donating ability between 2-CP intermediates and 2-CP in the reaction (Fig. 2d). The results showed that the reacted suspension of MZS/ H_2O_2 /2-CP intermediates possessed a lower charge transfer resistance, indicating easier charge transfer in this system, and thus the 2-CP intermediates have a stronger electron donation capacity. To demonstrate that DO indeed participates in this 2e^- ORR process, degradation experiments under air and nitrogen (N_2) atmospheres (excluding part of O_2) were conducted. As presented in Fig. 2e, the introduction of N_2 barely affected the removal of pollutants, which was nearly completely degraded within 30 min. It was worth noting that the removal of pollutants over the first 2 min was significantly faster under a N_2 atmosphere than in air. Combined with the analysis of the H_2O_2 concentration histogram, which may be the result of the low DO content in the N_2 atmosphere within the first 2 min, the electrons donated by the pollutants were more available for the reduction of H_2O_2 to produce $\cdot\text{OH}$ than for the ORR process (Fig. 2f). In the air atmosphere, the electrons from pollutants were more available for the

ORR process, resulting in more H_2O_2 generation. Furthermore, the H_2O_2 concentration remained at a high level in both air and in N_2 with clearly observable sawtooth fluctuations throughout the process, which was the combined effects of pollutant electron donation and the 2e^- ORR process.

Significant H_2O_2 generation was still observed in the MZS/ H_2O_2 system (2 mM), and the H_2O_2 concentration decreased sharply with the accumulation of intermediates (Fig. 2g). At 30 min, H_2O_2 concentrations in the ECs/actual wastewater system were found to be significantly higher than those in the RhB system, indicating that MZS/ H_2O_2 could effectively utilize the electrons in actual wastewater (Fig. 2h). Furthermore, the highest H_2O_2 concentration was observed in the BPA/CIP/wastewater system, demonstrating that the synergistic interaction between ECs may promote electron transfer. Similarly, the electron donation effect of pollutants in industrial wastewater was investigated (Fig. 2i). Compared to the rapid decomposition of H_2O_2 in UP water, the decomposition of H_2O_2 in actual wastewater was ineffective and significantly slower, proving the effective utilization of pollutant electrons in wastewater on this confined nonequilibrium surface.

3.3. Construction of a confined nonequilibrium surface

Scanning electron microscopy (SEM) revealed that MZS generally exhibited pomegranate-like spheres 5–6 μm in diameter arranged in a large number of nanoparticle stacks (Fig. S7 a, b and c). SEM mappings

of MZS confirmed the presence of Zn, S, and Mo elements as well as the good dispersion of the three elements indicating that Mo doping did not lead to the formation of sulfide clusters (Fig. S7d). The results of transmission electron microscopy (TEM) further indicated that MZS possessed a microsphere structure with lamellar skeletons resulting from the formation of Mo-S bonds (Fig. S8). Two distinctly categories of lattice stripes could be observed in the high-resolution TEM (HRTEM) images (Fig. S9). Coarse stripes with an interlayer distance of 0.64 nm were attributed to the (002) crystalline plane of MoS₂, demonstrating the well-ordered growth of Mo in this direction [46]. An additional dense lattice stripe with a lattice spacing of 0.32 nm affiliated with hexagonal ZnS (002) crystalline planes that match the principal crystalline phase characteristic of MZS [47] could also be observed.

Powder X-ray diffraction (XRD) patterns of the synthesized ZnS and MZS composites are presented in Fig. 3a. For pure ZnS, the diffraction peaks at 28.70 and 33.25 degrees corresponded to the (111) and (200) crystal planes of typical cubic sphalerite, respectively (Fig. 3a inset) [48,49]. The doping of Mo drastically changed the structure of ZnS, not only shifting the diffraction peaks of the original cubic crystal but also causing lattice phase transition, with the appearance of the (100) and (101) crystal planes of hexagonal ZnS (26.94° and 30.46°) [50]. Furthermore, a novel feature which has never been previously reported, emerged in the form of a peak located at 14.07° and was attributed to the typical hexagonal MoS₂ (002) crystal plane. No other peaks were observed, confirming that Mo only grew in situ along the hexagonal (002) crystal plane [51] (Fig. S10). The microstructure of MZS was further investigated by means of Raman spectroscopy. As shown in Fig. 3b, the peaks in MZS with Raman shifts at 204.2 cm⁻¹ and 335.5 cm⁻¹ were attributed to the vibrations of the Zn-S bond, while the peaks located at 372.9 cm⁻¹ and 401.3 cm⁻¹ were attributed to Mo-S bond vibrations [52]. The above structural characterization provided strong evidence of the lattice phase transition and the formation of

Mo-S-Zn bridges in the prepared catalysts.

Electron paramagnetic resonance (EPR) techniques were employed to investigate the influence of Mo doping on electron distribution. For pure ZnS, six single electron signals were observed, having similar intensity and equal spacing, and being highly regular and tightly unavailable (Fig. 3c inset). In contrast, the doping of Mo disrupted the inherently regular electron arrangement and allowed it to be utilized via activation, resulting in the appearance of six equally spaced single-electron signals of varying intensity in the g-value range of 1.88–2.14. The electron rearrangement of MZS was further confirmed by X-ray photoelectron spectroscopy (XPS). Based on the position and shape of the 3d and S 2p spectra, it could be concluded that Mo mainly formed Mo-S bonds in the form of Mo⁴⁺ (Fig. S11). Compared to that of Zn, the position of the main peak of Zn 2p in MZS was shifted significantly, by as much as 0.5 eV, toward higher binding energy. This was due to the electronegativity difference allowing part of the electrons belonging to Zn to be transferred to the Mo sites via the Zn-S-Mo bridge, resulting in a stronger binding force of Zn sites for the remaining electrons (Fig. 3d) [53]. Moreover, the electron transfers also led to the formation of poor/rich DRCs in the confined nonequilibrium surface. To further investigate the effect of Mo doping on the surface electron arrangement, corresponding DFT calculations were performed. For the optimized crystal configuration, the monolayer ZnS crystals were arranged in a regular pattern with a uniform electron distribution, while Mo doping disrupted the original uniform structure and rearranged the electrons to form DRCs (Fig. 3e). The significant gap between the local potential of −55.8 eV at the Mo site and −14.4 eV at the adjacent Zn site demonstrated the difference in the electron-binding capacity (Fig. 3f) [54]. In addition, the presence of significant spin electron density at the Mo site implied that this site may possess strong catalytic activity. These results verified the formation of DRCs on the confined nonequilibrium surface.

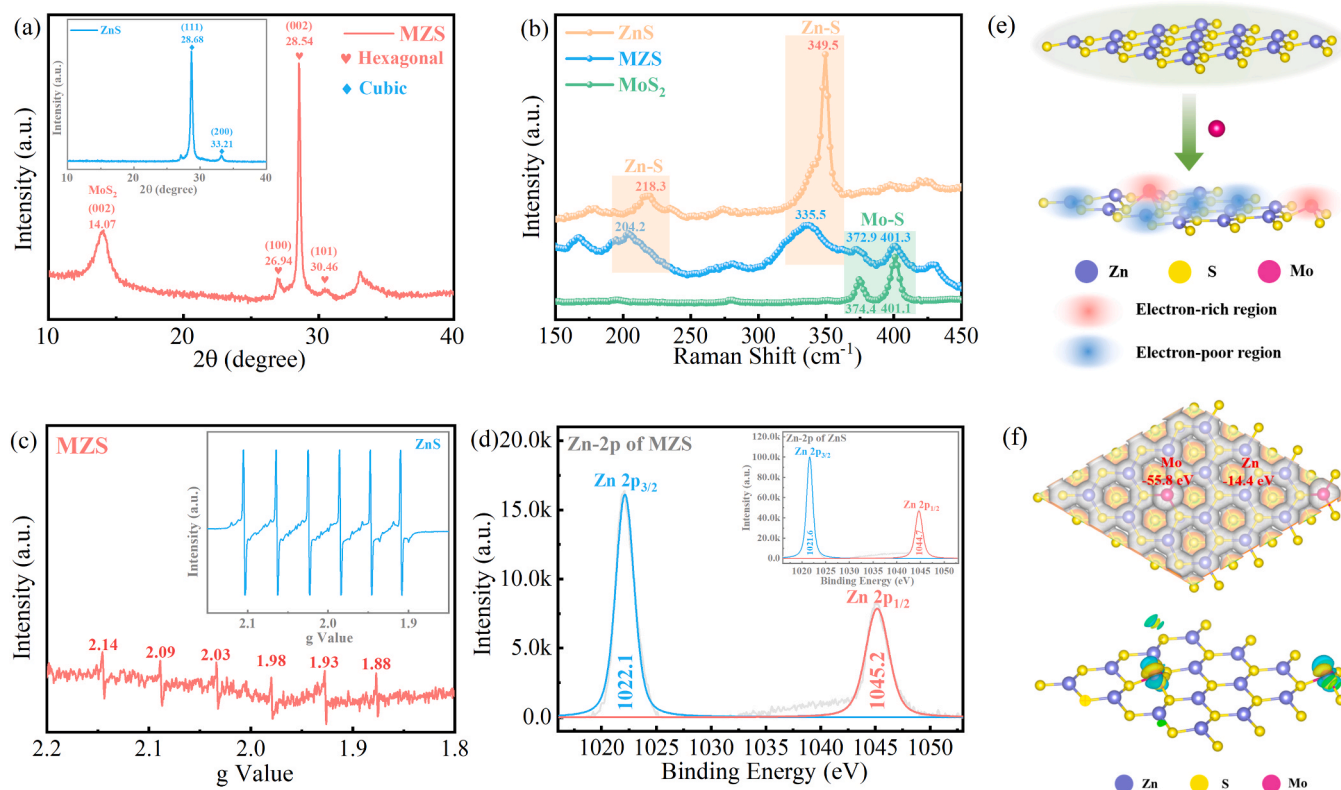


Fig. 3. (a) XRD pattern of MZS (the insert shows the XRD pattern of ZnS). (b) Raman spectra of ZnS, MoS₂ and MZS. (c) Solid EPR spectrum of MZS (the insert shows the solid EPR spectrum of ZnS). (d) Zn 2p XPS spectrum of MZS (the insert shows the Zn 2p XPS spectrum of ZnS). (e) The differences in the surface electron distributions of MZS and ZnS calculated by DFT. (f) Local potential and spin electron density of MZS calculated by DFT.

3.4. Interfacial mechanism of trace H_2O_2 triggering H_2O_2 generation through ECs utilization on a confined nonequilibrium surface

The interfacial mechanism of trace H_2O_2 triggering H_2O_2 generation through pollutant utilization on a confined nonequilibrium surface was explored. Fig. 4a showed the multiplication of single electrons after the interaction of MZS with RhB, indicating the successful transfer of pollutant electrons to the confined nonequilibrium surface and serving as the electron donor for the reaction system. ROS generated in various MZS/ H_2O_2 systems was characterized in order to reveal the electron transfer pathways between the catalyst, H_2O_2 , and DO. Fig. 4b and Fig. 4c present the BMPO- $\cdot\text{OH}$ and BMPO- $\text{O}_2^{\cdot-}$ signals, respectively. In the absence of pollutants, MZS was able to interact with H_2O_2 by itself to produce a relatively weak 1:2:2:1 $\cdot\text{OH}$ signal and a distinct four-equivalent $\text{O}_2^{\cdot-}$ signal. The difference in the intensity of the two signals was attributed to the fact that MZS alone could provide only a few electrons for the reduction of H_2O_2 to produce $\cdot\text{OH}$, while H_2O_2 was prone to lose electrons and to be oxidized to $\text{O}_2^{\cdot-}$. The shape and position of these two signals did not change with the addition of RhB, while the BMPO- $\cdot\text{OH}$ signal was enhanced and the BMPO- $\text{O}_2^{\cdot-}$ signal was weakened exponentially. The addition of pollutants constantly supplied electrons to the system, resulting in an easier process for H_2O_2 to be reduced to $\cdot\text{OH}$ rather than be oxidized to $\text{O}_2^{\cdot-}$, while $\text{O}_2^{\cdot-}$ was mostly generated by DO gaining electrons through the ORR process. The TEMP- $^1\text{O}_2$ signals acquired with and without pollutants indicated that the MZS/ H_2O_2 system could not only utilize the pollutant electrons for the ORR process but could also effectively utilize the pollutant energy for the excitation of ground state O_2 to generate the excited state, $^1\text{O}_2$ (Fig. 4d). To further verify the triggering effect of H_2O_2 on the $2e^-$ ORR process, DFT calculations were performed to investigate the interfacial interactions of H_2O_2 at different active sites on the confined nonequilibrium surface. As shown in Fig. 4e, the interfacial binding energy (IBE) for the adsorption of H_2O_2 onto a single Zn site was observed to be -5.93 eV. The $\text{O}=\text{O}$ bond length of 3.55 Å was much longer than the $\text{O}=\text{O}$ bond length in H_2O_2 , indicating that H_2O_2 could spontaneously adsorb onto the Zn site and be easily activated to ROS. In contrast, the IBE for H_2O_2 adsorption onto the Mo site was -7.32 eV and much larger

in absolute value than that at the Zn site, indicating the preference for and stable adsorption of H_2O_2 onto the Mo site. This was confirmed by the direct breakage of the $\text{O}=\text{O}$ bond (2.93 Å) and high spin electron density of H_2O_2 after decomposition at the Mo site (Fig. 4f).

In situ Raman spectroscopy was used to investigate the interfacial competitive adsorption processes of H_2O_2 and ECs at the confined nonequilibrium surface. BPA was selected as the target contaminant for *in situ* Raman test because it has no fluorescence interference signal. In the absence of pollutants, the $\text{O}=\text{O}$ bond at a Raman shift of 874.25 cm^{-1} was observed after the addition of H_2O_2 , demonstrating that H_2O_2 was stably adsorbed onto the confined nonequilibrium surface (Fig. 5a). Furthermore, there was no significant weakening or shift of the signal over time, indicating that the H_2O_2 in the system could exist relatively stable. Upon the addition of the pollutants to the system, the peak position of the $\text{O}=\text{O}$ bond shifted slightly (874.25 – 872.57 cm^{-1}), indicating the existence of competitive adsorption between H_2O_2 and the pollutant (Fig. 5b). Moreover, the intensity and position of the signal did not change over time. Combined with the pollutant and H_2O_2 concentration curves, these results verified H_2O_2 generation via the $2e^-$ ORR process utilizing pollutant electrons at the confined nonequilibrium surface. Subsequently, the cyclic voltammetry curves of MZS were tested to investigate the promoting effect of H_2O_2 on the electron cycling of pollutants at the confined nonequilibrium surface. As presented in Fig. 5c, the curve tended to close, and the redox potential decreased with the addition of H_2O_2 , indicating that H_2O_2 accelerated the cycling of electrons inside the system. This caused the $2e^-$ ORR process to be more intense and improved H_2O_2 generation. Free radical inhibition experiments were employed to clarify the main active species in the reaction. As shown in Fig. 5d, with the addition of *p*-BQ, IPA, or L-histidine, the degradation of pollutant was inhibited. The percentage of free radicals that contributed to the degradation was considered to be the percentage of the pollutants remaining in the system with each inhibitor at 30 min. The results suggested that $^1\text{O}_2$ inhibited by L-histidine contributed the most, at approximately 55 %, to the degradation reaction, and acted as the main active species in the reaction system. $\text{O}_2^{\cdot-}$ inhibited by BQ contributed approximately 35 % to the degradation reaction, while $\cdot\text{OH}$ inhibited by IPA and organic radical intermediates contributed the least

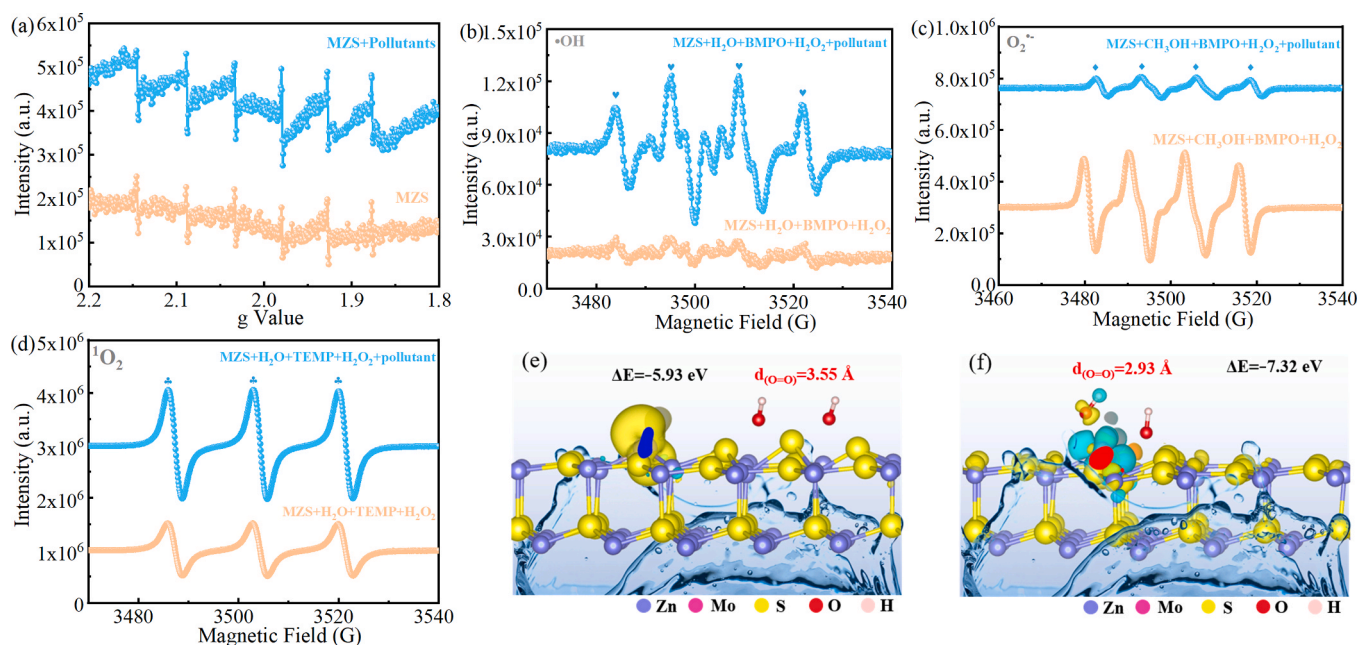


Fig. 4. (a) Solid EPR of MZS and MZS after reaction with pollutant. BMPO spin-trapping EPR spectra for (b) $\cdot\text{OH}$ in various aqueous suspensions with H_2O_2 and (c) $\text{HO}_2^{\cdot}/\text{O}_2^{\cdot-}$ in various methanol suspensions with H_2O_2 . TEMP spin-trapping EPR spectra for (d) $^1\text{O}_2$ in various aqueous suspensions with H_2O_2 . Optimized adsorption/reaction model for H_2O_2 at a (e) Zn site and (f) Mo site on the surface of MZS obtained via DFT calculation. Purple, rose, yellow, light pink, and red balls represent Zn, Mo, S, C, H, and O, respectively.

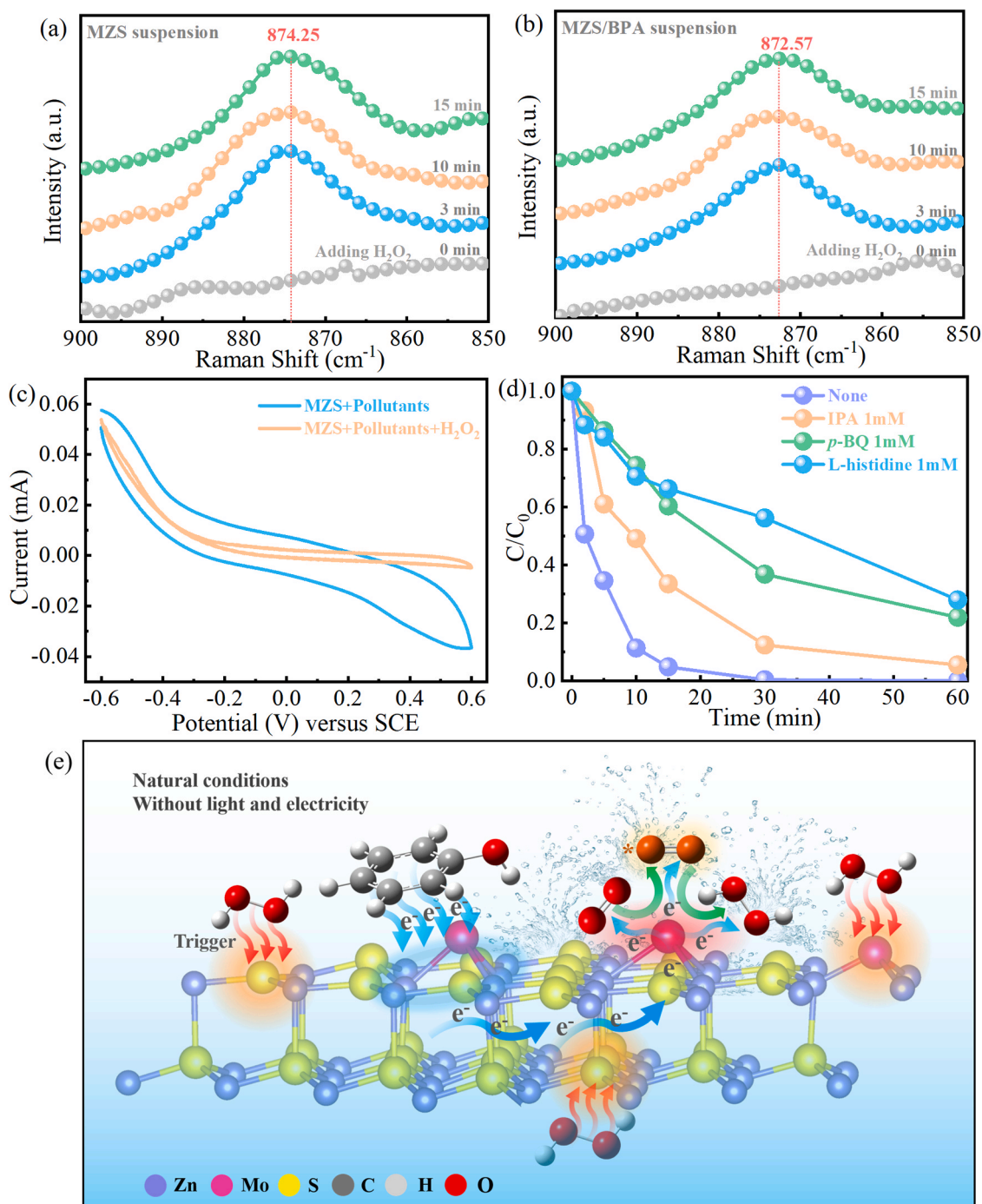


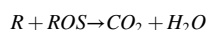
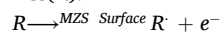
Fig. 5. *In situ* Raman spectra of (a) various aqueous suspensions and (b) various pollutant suspensions. (c) CV curves of MZS in various aqueous suspensions with RhB. (d) Effect of different inhibitors on the degradation of RhB in the MZS/H₂O₂ system. (e) Schematic of trace H₂O₂ triggering H₂O₂ generation through pollutant utilization on a confined nonequilibrium surface. Reaction conditions: [catalyst] = 0.2 g/L, [H₂O₂] = 10 mM, [pollutant] = 10 mg/L 50 mL, initial pH, [IPA] = 1 mM, [p-BQ] = 1 mM, [L-histidine] = 1 mM.

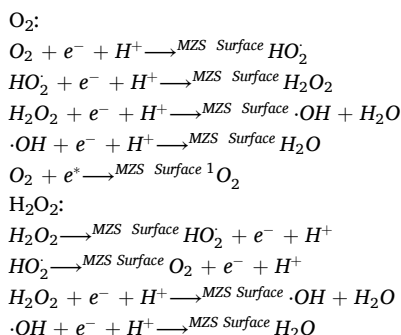
(~10 %).

Based on the above conclusions, one could accurately speculate on the interface processes of ECs, DO, and H₂O₂ at the confined nonequilibrium surface (Fig. 5e). First, trace amounts of H₂O₂ adsorbed onto the Mo or Zn site were decomposed and activated to ROS to trigger the reaction. Then, partial ROS were consumed by attacking the ECs, and the remaining O₂^{•-} and DO gained electrons at the Mo sites to produce H₂O₂ through the 2e⁻ ORR process to maintain the dynamic equilibrium of the H₂O₂ concentration. In addition, the ECs that were adsorbed onto the surface transferred to MZS electrons which were further stored at the

confined nonequilibrium surface as temporary residents and subsequently utilized for H₂O₂ generation. Thus, the removal of ECs consists of two stages, with a significant number of ECs being attacked by ROS and a small amount being progressively degraded by resource utilization. The specific electron transfer and radical generation reaction equations are as follows:

ECs(R):





4. Conclusion

In summary, we developed a DRC catalyst MZS with a confined nonequilibrium surface to solve the bottleneck of high energy consumption for water purification and ORR process by utilizing pollutant electrons and energy. It was found that efficient H_2O_2 generation and pollutant degradation were achieved without light and electricity by replacing conventional sacrificial agents with pollutant electrons under the trigger of trace H_2O_2 . Structural characterization revealed the successful construction of DRCs on the confined non-equilibrium surface and the extremely strong ability of the Mo site to gain electrons, which was the key to good catalytic activity of MZS as well as the excellent ORR performance. In the actual reaction, pollutant electrons as spontaneous electron donors were efficiently used for ORR process on the confined non-equilibrium surface, while the generated H_2O_2 was utilized for pollutant degradation, which greatly reduced the energy consumption for water treatment. This work brought new insights to the low-energy consumption water purification and $2e^-$ ORR process, which achieved harmlessness and resourcefulness of pollutants simultaneously.

CRedit authorship contribution statement

Chao Lu: Conceptualization, Methodology, Investigation, Data curation, Formal analysis, Visualization, and Writing-original draft. **Chun Hu:** Supervision, Validation, Funding acquisition, and Project administration. **Hongwei Rong:** Supervision and Validation. **Lai Lyu:** Conceptualization, Supervision, Visualization, Formal analysis, Methodology, Writing-review & editing, Funding acquisition and Supervision.

Declaration of Competing Interest

The authors declare that they have no known competing financial interests or personal relationships that could have appeared to influence the work reported in this paper.

Data availability

Data will be made available on request.

Acknowledgements

This work was financially supported by the Introduced Innovative R&D Team Project under the "Pearl River Talent Recruitment Program" of Guangdong Province (2019ZT08L387), the Natural Science Foundation of China (52070046, 52122009, 51838005, 52150056) and the Basic and Applied Basic Research Project of Guangzhou (202201020163).

Appendix A. Supporting information

Supplementary data associated with this article can be found in the online version at [doi:10.1016/j.apcatb.2023.123051](https://doi.org/10.1016/j.apcatb.2023.123051).

References

- [1] A. Alsaiee, B.J. Smith, L.L. Xiao, Y.H. Ling, D.E. Helbling, W.R. Dichtel, Rapid removal of organic micropollutants from water by a porous β -cyclodextrin polymer, *Nature* 529 (2016) 190–194.
- [2] R.P. Schwarzenbach, B.I. Escher, K. Fenner, T.B. Hofstetter, C.A. Johnson, U. von Gunten, B. Wehrli, The challenge of micropollutants in aquatic systems, *Science* 313 (2006) 1072–1077.
- [3] B. Wang, G. Yu, Emerging contaminant control: From science to action, *Front. Env. Sci. Eng.* 16 (2022) 81.
- [4] J. Wu, J. Lu, J. Wu, Effect of gastric fluid on adsorption and desorption of endocrine disrupting chemicals on microplastics, *Front. Env. Sci. Eng.* 16 (2022) 104.
- [5] M. Ahmed, M.O. Mavukkandy, A. Giwa, M. Elektrowicz, E. Katsou, O. Khelifi, V. Naddeo, S.W. Hasan, Recent developments in hazardous pollutants removal from wastewater and water reuse within a circular economy, *npj Clean Water* 5 (2022) 12.
- [6] O.S. Arvaniti, M.E. Dasenaki, A.G. Asimakopoulos, N.C. Maragou, V.G. Samaras, K. Antoniou, G. Gatidou, D. Mamais, C. Noutsopoulos, Z. Frontistis, N. S. Thomaidis, A.S. Stasinakis, Effectiveness of tertiary treatment processes in removing different classes of emerging contaminants from domestic wastewater, *Front. Env. Sci. Eng.* 16 (2022) 148.
- [7] T.T. Gao, C. Lu, C. Hu, L. Lyu, H_2O_2 inducing dissolved oxygen activation and electron donation of pollutants over Fe-ZnS quantum dots through surface electron-poor/rich microregion construction for water treatment, *J. Hazard. Mater.* 420 (2021), 126579.
- [8] K.L. Deng, Y.T. Gu, T.T. Gao, Z.Y. Liao, Y.X. Feng, S. Zhou, Q. Fang, C. Hu, L. Lyu, Carbonized MOF-coated zero-valent Cu driving an efficient dual-reaction-center Fenton-like water treatment process through utilizing pollutants and natural dissolved oxygen, *ACS EST Water* 2 (2022) 174–183.
- [9] S.Y. Zhao, C.X. Chen, J. Ding, S.S. Yang, Y.N. Zang, N.Q. Ren, One-pot hydrothermal fabrication of $BiVO_4/Fe_3O_4/rGO$ composite photocatalyst for the simulated solar light-driven degradation of Rhodamine B, *Front. Env. Sci. Eng.* 16 (2022) 36.
- [10] Y. Yang, Q. Zhang, B.Y. Chen, L.C. Long, G. Zhang, Toward better understanding vacuum ultraviolet-iodide induced photolysis via hydrogen peroxide formation, iodine species change, and difluoroacetic acid degradation, *Front. Env. Sci. Eng.* 16 (2022) 55.
- [11] L.H. Gao, Y.J. Cao, L.Z. Wang, S.L. Li, A review on sustainable reuse applications of Fenton sludge during wastewater treatment, *Front. Env. Sci. Eng.* 16 (2022) 77.
- [12] C. Lu, K.L. Deng, C. Hu, L. Lyu, Dual-reaction-center catalytic process continues Fenton's story, *Front. Env. Sci. Eng.* 14 (2020) 82.
- [13] N. Agarwal, S.J. Freakley, R.U. McKiver, S.M. Althabhan, N. Dimitratos, Q. He, D. J. Morgan, R.L. Jenkins, D.J. Willock, S.H. Taylor, C.J. Kiely, G.J. Hutchings, Aqueous Au-Pd colloids catalyze selective CH_4 oxidation to CH_3OH with O_2 under mild conditions, *Science* 358 (2017) 223–227.
- [14] R. Hage, A. Lienke, Applications of transition-metal catalysts to textile and wood-pul bleaching, *Angew. Chem. Int. Edit.* 45 (2006) 206–222.
- [15] D.M. Schultz, T.P. Yoon, Solar synthesis: Prospects in visible light photocatalysis, *Science* 343 (2014) 1239176.
- [16] K. Mase, M. Yoneda, Y. Yamada, S. Fukuzumi, Seawater usable for production and consumption of hydrogen peroxide as a solar fuel, *Nat. Commun.* 7 (2016) 11470.
- [17] J.M. Campos-Martin, G. Blanco-Brieva, J.L.G. Fierro, Hydrogen peroxide synthesis: An outlook beyond the anthraquinone process, *Angew. Chem. Int. Edit.* 45 (2006) 6962–6984.
- [18] J.K. Edwards, B. Solsona, Edwin Ntainjua N, A.F. Carley, A.A. Herzing, C.J. Kiely, G.J. Hutchings, Switching off hydrogen peroxide hydrogenation in the direct synthesis process, *Science* 323 (2009) 1037–1041.
- [19] J.K. Edwards, E. Ntainjua, A.F. Carley, A.A. Herzing, C.J. Kiely, G.J. Hutchings, Direct synthesis of H_2O_2 from H_2 and O_2 over gold, palladium, and gold-palladium catalysts supported on acid-pretreated TiO_2 , *Angew. Chem. Int. Edit.* 48 (2009) 8512–8515.
- [20] C. Xia, Y. Xia, P. Zhu, L. Fan, H.T. Wang, Direct electrosynthesis of pure aqueous H_2O_2 solutions up to 20% by weight using a solid electrolyte, *Science* 366 (2019) 226–231.
- [21] N.M. Wilson, D.W. Flaherty, Mechanism for the direct synthesis of H_2O_2 on Pd clusters: Heterolytic reaction pathways at the liquid-solid interface, *J. Am. Chem. Soc.* 138 (2016) 574–586.
- [22] F.T. Wang, Y.P. Zhou, S. Lin, L.J. Yang, Z. Hu, D.Q. Xie, Axial ligand effect on the stability of Fe-N-C electrocatalysts for acidic oxygen reduction reaction, *Nano Energy* 78 (2020), 105128.
- [23] N. Wang, S.B. Ma, P.J. Zuo, J.Z. Duan, B.R. Hou, Recent progress of electrochemical production of hydrogen peroxide by two-electron oxygen reduction reaction, *Adv. Sci.* 8 (2021) 2100076.
- [24] Y.Y. Pang, H. Xie, Y. Sun, M.M. Titirici, G.L. Chai, Electrochemical oxygen reduction for H_2O_2 production: catalysts, pH effects and mechanisms, *J. Mater. Chem. A* 8 (2020) 24996–25016.
- [25] K. Wang, Z.H. Mo, S.T. Tang, M.Y. Li, H. Yang, B. Long, Y. Wang, S.Q. Song, Y. X. Tong, Photo-enhanced Zn-air batteries with simultaneous highly efficient in situ H_2O_2 generation for wastewater treatment, *J. Mater. Chem. A* 7 (2019) 14129–14135.
- [26] C. Krishnaraj, H.S. Jena, L. Bourda, A. Laemont, P. Pachfule, J. Roesser, C. V. Chandran, S. Borgmans, S.M.J. Rogge, K. Leus, C.V. Stevens, J.A. Martens, V. Van Speybroeck, E. Breynaert, A. Thomas, P. Van der Voort, Strongly reducing (diarylamino) benzene-based covalent organic framework for metal-free visible light photocatalytic H_2O_2 generation, *J. Am. Chem. Soc.* 142 (2020) 20107–20116.

- [27] O.Y. Jung, M.L. Pegis, Z.X. Wang, G. Banerjee, C.T. Nemes, W.L. Hoffeditz, J. T. Hupp, C.A. Schmuttenmaer, G.W. Brudvig, J.M. Mayer, Highly active NiO photocathodes for H_2O_2 production enabled via outer-sphere electron transfer, *J. Am. Chem. Soc.* 140 (2018) 4079–4084.
- [28] K.L. Cao, H. Yang, S.X. Bai, Y. Xu, C.Y. Yang, Y. Wu, M. Xie, T. Cheng, Q. Shao, X. Q. Huang, Efficient direct H_2O_2 synthesis enabled by PdPb nanorings via inhibiting the O-O bond cleavage in O_2 and H_2O_2 , *ACS Catal.* 11 (2021) 1106–1118.
- [29] H.N. Che, X. Gao, J. Chen, J. Hou, Y.H. Ao, P.F. Wang, Iodide-induced fragmentation of polymerized hydrophilic carbon nitride for high-performance quasi-homogeneous photocatalytic H_2O_2 production, *Angew. Chem. Int. Edit.* 60 (2021) 25546–25550.
- [30] T.H. Jeon, B. Kim, C. Kim, C. Xia, H.T. Wang, P.J.J. Alvarez, W. Choi, Solar photoelectrochemical synthesis of electrolyte-free H_2O_2 aqueous solution without needing electrical bias and H_2 dagger, *Energy Environ. Sci.* 14 (2021) 3110–3119.
- [31] T.H. Jeon, H. Kim, H.I. Kim, W. Choi, Highly durable photoelectrochemical H_2O_2 production via dual photoanode and cathode processes under solar simulating and external bias-free conditions, *Energy Environ. Sci.* 13 (2020) 1730–1742.
- [32] C. Chu, Q. Li, W. Miao, H. Qin, X. Liu, D. Yao, S. Mao, Photocatalytic H_2O_2 production driven by cyclodextrin-pyrimidine polymer in a wide pH range without electron donor or oxygen aeration, *Appl. Catal. B Environ.* 314 (2022), 121485.
- [33] Q. You, C. Zhang, M. Cao, B. Wang, J. Huang, Y. Wang, S. Deng, G. Yu, Defects controlling, elements doping, and crystallinity improving triple-strategy modified carbon nitride for efficient photocatalytic diclofenac degradation and H_2O_2 production, *Appl. Catal. B Environ.* (2022), 121941.
- [34] L. Lyu, D.B. Yan, G.F. Yu, W.R. Cao, C. Hu, Efficient destruction of pollutants in water by a dual-reaction center Fenton-like process over carbon nitride compounds-complexed Cu(II)-CuAlO₂, *Environ. Sci. Technol.* 52 (2018) 4294–4304.
- [35] L. Lyu, G.F. Yu, L.L. Zhang, C. Hu, Y. Sun, 4-phenoxyphenol-functionalized reduced graphene oxide nanosheets: A metal-free Fenton-like catalyst for pollutant destruction, *Environ. Sci. Technol.* 52 (2018) 747–756.
- [36] L. Lyu, L.L. Zhang, Q.Y. Wang, Y.L. Nie, C. Hu, Enhanced Fenton catalytic efficiency of $\gamma\text{-Cu-Al}_2\text{O}_3$ by $\delta\text{-Cu}^{2+}$ -ligand complexes from aromatic pollutant degradation, *Environ. Sci. Technol.* 49 (2015) 8639–8647.
- [37] Y.M. Wang, L. Lyu, D. Wang, H.Q. Yu, T. Li, Y.W. Gao, F. Li, J.C. Crittenden, L. L. Zhang, C. Hu, Cation- π induced surface cleavage of organic pollutants with $\bullet\text{OH}$ formation from H_2O for water treatment, *iScience* 24 (2021), 102874.
- [38] S.H. Zhan, H.X. Zhang, X.Y. Mi, Y.B. Zhao, C. Hu, L. Lyu, Efficient Fenton-like process for pollutant removal in electron-rich/poor reaction sites induced by surface oxygen vacancy over cobalt-zinc oxides, *Environ. Sci. Technol.* 54 (2020) 8333–8343.
- [39] L. Lyu, W.R. Cao, G.F. Yu, D.B. Yan, K.L. Deng, C. Lu, C. Hu, Enhanced polarization of electron-poor/rich micro-centers over nZVCu-Cu(II)-rGO for pollutant removal with H_2O_2 , *J. Hazard. Mater.* 383 (2020), 121182.
- [40] L. Lyu, L.L. Zhang, G.Z. He, H. He, C. Hu, Selective H_2O_2 conversion to hydroxyl radicals in the electron-rich area of hydroxylated C-g-C₃N₄/CuCo-Al₂O₃, *J. Mater. Chem. A* 5 (2017) 7153–7164.
- [41] W.R. Cao, L. Lyu, K.L. Deng, C. Lu, C. Hu, L-ascorbic acid oxygen-induced micro-electronic fields over metal-free polyimide for peroxymonosulfate activation to realize efficient multi-pathway destruction of contaminants, *J. Mater. Chem. A* 8 (2020) 810–819.
- [42] L. Lyu, M.E. Han, W.R. Cao, Y.W. Gao, Q.Y. Zeng, G.F. Yu, X. Huang, C. Hu, Efficient Fenton-like process for organic pollutant degradation on Cu-doped mesoporous polyimide nanocomposites, *Environ. Sci. Nano* 6 (2019) 798–808.
- [43] M.E. Han, L. Lyu, Y.M. Huang, J.R. Liang, M.M. Xue, T. Wu, J.Y. Li, M.P. Chen, C. Hu, In situ generation and efficient activation of H_2O_2 for pollutant degradation over CoMoS₂ nanosphere-embedded rGO nanosheets and its interfacial reaction mechanism, *J. Colloid Interf. Sci.* 543 (2019) 214–224.
- [44] M. Cargnello, J.J.D. Jaen, J.C.H. Garrido, K. Bakhmutsky, T. Montini, J.J. C. Gamez, R.J. Gorte, P. Fornasiero, Exceptional activity for methane combustion over modular Pd/CeO₂ subunits on functionalized Al₂O₃, *Science* 337 (2012) 713–717.
- [45] M.R. Wu, S.L. Song, T.Y. Wang, W. Sun, S.M. Xu, Y. Yang, Natural sphalerite photocatalyst for treatment of oily wastewater produced by solvent extraction from spent lithium-ion battery recycling, *Appl. Catal. B Environ.* 313 (2022), 121460.
- [46] J.M. Wu, W.E. Chang, Y.T. Chang, C.K. Chang, Piezo-catalytic effect on the enhancement of the ultra-high degradation activity in the dark by single- and few-layers MoS₂ nanoflowers, *Adv. Mater.* 28 (2016) 3718–3725.
- [47] Y. Liao, H. Xu, W. Liu, H. Ni, X. Zhang, A. Zhai, Z. Quan, Z. Qu, N. Yan, One step interface activation of ZnS using cupric ions for mercury recovery from nonferrous smelting flue gas, *Environ. Sci. Technol.* 53 (2019) 4511–4518.
- [48] W. Luo, J. Zhang, M. Li, A. Züttel, Boosting CO production in electrocatalytic CO₂ reduction on highly porous Zn catalysts, *ACS Catal.* 9 (2019) 3783–3791.
- [49] I. Sorribes, L.C. Liu, A. Corma, Nanolayered Co-Mo-S catalysts for the chemoselective hydrogenation of nitroarenes, *ACS Catal.* 7 (2017) 2698–2708.
- [50] A. Fairbrother, E. Garcia-Hemme, V. Izquierdo-Roca, X. Fontane, F.A. Pulgarin-Agudelo, O. Vigil-Galan, A. Perez-Rodriguez, E. Saucedo, Development of a selective chemical etch to improve the conversion efficiency of Zn-rich Cu₂ZnSnS₄ solar cells, *J. Am. Chem. Soc.* 134 (2012) 8018–8021.
- [51] X.Y. Yu, H. Hu, Y.W. Wang, H.Y. Chen, X.W. Lou, Ultrathin MoS₂ nanosheets supported on N-doped carbon nanoboxes with enhanced lithium storage and electrocatalytic properties, *Angew. Chem. Int. Edit.* 54 (2015) 7395–7398.
- [52] J.T. Zhu, H. Xu, G.F. Zou, W. Zhang, R.Q. Chai, J. Choi, J. Wu, H.Y. Liu, G.Z. Shen, H.Y. Fan, MoS₂-OH bilayer-mediated growth of inch-sized monolayer MoS₂ on arbitrary substrates, *J. Am. Chem. Soc.* 141 (2019) 5392–5401.
- [53] J. Sun, H. Xue, N.K. Guo, T.S. Song, Y.R. Hao, J.W. Sun, J.W. Zhang, Q. Wang, Synergetic metal defect and surface chemical reconstruction into NiCo₂S₄/ZnS heterojunction to achieve outstanding oxygen evolution performance, *Angew. Chem. Int. Edit.* 60 (2021) 19435–19441.
- [54] C. Lu, Q. Fang, C. Hu, L. Lyu, Sustainable micro-activation of dissolved oxygen driving pollutant conversion on Mo-enhanced zinc sulfide surface in natural conditions, *Fund. Res.* 3 (2023) 422–429.